Impact of gravity and inertia on stable displacements of DNAPL in highly permeable porous media

Maxime Cochennec, Hossein Davarzani, Yohan Davit, Stéfan Colombano, Ioannis Ignatiadis, Guillaume Masselot, Michel Quintard

To cite this version:

Maxime Cochennec, Hossein Davarzani, Yohan Davit, Stéfan Colombano, Ioannis Ignatiadis, et al.. Impact of gravity and inertia on stable displacements of DNAPL in highly permeable porous media. Advances in Water Resources, 2022, 162, pp.104139. ⟨10.1016/j.advwatres.2022.104139⟩. ⟨hal-03854229⟩

HAL Id: hal-03854229
https://hal.science/hal-03854229v1

Submitted on 15 Nov 2022

Impact of gravity and inertia on stable displacements of DNAPL in highly permeable porous media

Maxime Cochennec[a,b,c], Hossein Davarzani[b,*], Yohan Davit[c], Stéfan Colombano[b], Ioannis Ignatiadis[b], Guillaume Masselot[a], Michel Quintard[c]

[a] *Agence de la transition écologique (ADEME), Angers, France*
[b] *French Geological Survey (BRGM), Orléans, France*
[c] *Institut de Mécanique des Fluides de Toulouse (IMFT), Université de Toulouse, CNRS, France*

Abstract

The flow of Dense Non-Aqueous Phase Liquid (DNAPL) in highly permeable porous media is characterized by a complex interplay between surface tension, viscous, gravity, and inertia forces. Gravitational effects in these systems have been particularly studied in the context of displacement instability, but little work has focused on the impact of gravitational and inertia forces on the stable displacement of DNAPL in highly permeable but non-fractured porous media. Here, we study the impact of the gravity and Forchheimer numbers on the stable displacement of DNAPL fronts in porous media. We first performed DNAPL injection experiments in bead packings of different sizes for different inlet flow rates and initial saturation. These experiments were accurately modeled using a Darcy-Forchheimer model combined with an Arbitrary Lagrangian-Eulerian tracking of the DNAPL front. Once validated against stable injections in glass beads, the model was then used to

---

[*] Corresponding author
Email address: `h.davarzani@brgm.fr` (Hossein Davarzani)

Preprint submitted to Advances in Water Resources *December 17, 2021*

perform a broader parametric study than available with our experimental setup. We explored different injection and pumping scenarios over a range of dimensionless numbers. We found that gravity can significantly alter the fluid front in flows commonly found in contaminant hydrology. We estimate, however, that inertia will have a non-negligible impact upon the displacement of DNAPL only during active remediation techniques (e.g., free product pumping method) or pipe rupture events involving low-viscous DNAPL in highly-permeable porous media.

Keywords: Porous Media, Inertia, Gravity, Remediation, DNAPL

Nomenclature

Abbreviations

ALE	Arbitrary Lagrangian-Eulerian
DNAPL	Dense Non-Aqueous Phase Liquid
IBVP	Initial Boundary Value Problem
TDR	Time-Domain Reflectometer

Greek

η	Passability (m)
η_{ri}	Relative passability
μ	Dynamic viscosity (Pa s)
ϕ	Porosity
ρ	Density ($\mathrm{kg\,m^{-3}}$)
σ	Surface tension ($\mathrm{N\,m^{-1}}$)
θ	Contact angle (°)
ε	Permittivity

Latin

$\mathbf{F}_{ij}$	Inertial correction tensor
$\mathbf{K}_{ij}$	Multiphase permeability tensor ($\mathrm{m^2}$)
$\mathbf{V}$	Filtration velocity ($\mathrm{m\,s^{-1}}$)
$\mathbf{w}$	Macroscopic interface velocity ($\mathrm{m\,s^{-1}}$)
Bo	Bond number
Ca	Capillary number
d_b	Beads' diameter (m)
e	Eccentricity
F_o	Forchheimer number
G_r	Gravity number
K_0	Absolute permeability ($\mathrm{m^2}$)
k_{ri}	Relative permeability
P	Pressure (Pa)
P_c	Capillary pressure (Pa)
r_μ	Viscosity ratio
r_ρ	Density ratio
Re	Reynolds number
S	Saturation
S_{ei}	Irreducible saturation in ethanol
S_{or}	Residual saturation in oil
U	Characteristic velocity ($\mathrm{m\,s^{-1}}$)

1. Introduction

The flow of two immiscible fluids such as Dense Non-Aqueous Phase Liquid (DNAPL) and water in soils is ubiquitous in contaminant hydrology (Fetter et al., 1999). Our ability to model two-phase flows is important to estimate the spatio-temporal evolution of a pollutant and to evaluate the effectiveness of treatment strategies. Comparison between models and experiments have been proposed for different DNAPL's and flow scenario, including mercury (D'Aniello et al., 2018), PCE infiltration (Zheng et al., 2015), coal tar pumping (Colombano et al., 2020) or flow of a dense fluid that mimics DNAPL such as hydrofluoroether (Engelmann et al., 2021), to cite the most recent. However, two-phase flows in soils have been mostly studied in the context of petroleum extraction (Christie et al., 2001) and this literature inspired models used for DNAPL displacements (e.g. Abriola and Pinder (1985)). However, multiphase flows in petroleum engineering are different from those encountered in soil pollution applications. Porous media in oil reservoirs have in most cases a low permeability and are consolidated, whereas polluted aquifers are mostly unconsolidated and often highly permeable. Apart from soil remediation, two-phase flows in highly permeable porous media are common in hydrodynamics of packed-bed chemical reactors (de Santos et al., 1991; Attou et al., 1999) or in debris bed cooling of nuclear reactors (Tung and Dhir, 1988; Clavier et al., 2017).

In systems with high permeability and therefore larger characteristic pore sizes, viscous, gravity and inertia forces may dominate over capillary forces at pore-scale. The relative influence between these forces is captured by the capillary, Bond and Reynolds numbers. Tab. 1 gives typical values for these dimensionless numbers, either for two-phase flows in consolidated low permeability porous media (e.g. shale reservoir) or unconsolidated highly permeable porous media commonly encountered in aquifers (e.g. sandy soils) or chemical engineering (e.g. packed-bed reactors).

Porous media encountered in soil remediation include a wide range of permeability from about 1 darcy unit for fine sand to 10^6 darcy units for fractured rocks (1 darcy unit = 0.98×10^{-12} m^2). Here, we are interested in homogeneous unconsolidated porous media of absolute permeability between 300 and 3000 darcy units, which roughly corresponds to silty sand to fine gravels (Freeze and Cherry, 1979). Specifically, such values are often encountered in fluvioglacial deposits (Käser and Hunkeler, 2016; Vaudan et al., 2005; Nofal et al., 2019; Theel et al., 2020), and have also been studied in laboratory experiments involving DNAPL contamination (Yoon et al., 2009; Wilking et al., 2013). The effect of inertia on the displacement of DNAPL has been studied for flows in fractured rocks. For example, Ji et al. (2008) found a nonlinear relation between pressure gradient and filtration velocity starting at $Re \approx 10$ and a non-negligible impact on the flow. However, there is very little work on the effect of inertia on the displacement of DNAPL in highly permeable porous media. The issue is of interest because active remediation techniques (e.g., pumping) induce velocities that can be very large, especially in highly permeable media.

Finally, the interplay of different forces in highly permeable media has a direct impact on modeling. For stable flows (notion discussed in § 2.2), the fluid front may be sharp enough to justify modeling strategies based on an explicit description of the movement of a macroscopic front, rather than the

Table 1: Typical range of values for capillary, Bond and Reynolds numbers for different porous media. Modified from De Santos et al. (1991).

Porous media	$Ca = \frac{\text{viscosity}}{\text{capillary}}$	$Bo = \frac{\text{gravity}}{\text{capillary}}$	$Re = \frac{\text{inertia}}{\text{viscosity}}$
Consolidated	$10^{-7} - 10^{-3}$	$10^{-9} - 10^{-2}$	$10^{-9} - 10^{-2}$
Non-consolidated	$10^{-2} - 10$	$10^{-1} - 10$	$10^{-2} - 10^{2}$

traditional hyperbolic equation models that produce diffuse front solutions due to non-linear mobilities and, therefore, need constitutive relations. The interest of using a sharp front-tracking model is twofold: i) it is more representative of the experimentally observed front when the front is a clearly defined interface (which is the case in this study), ii) it only requires to know the residual saturation of the displacement to be modeled, and thus saves time compared to the drainage and imbibition cycles needed to find the parameters of the constitutive relations. This study develops such an explicit front displacement model to reproduce laboratory-scale experiments. We then use this model to study the effects of gravity and inertia upon the fluid front and to evaluate whether these effects can be encountered in real-life applications in contaminant hydrology. In addition, decimeter-scale experiments of stable injection in glass beads packing were carried out in laboratory to validate the mathematical model.

2. Theoretical background

Theoretical background for this work consists in two main part, namely the equations that govern the two-phase flow displacement with inertia and the stability of two-phase displacements. We summarily turn to both subjects in that respective order in the two following sections.

2.1. Governing equations for two-phase flows at Darcy-scale

Several macro-scale models describing two-phase flows in porous media including inertia effects have been proposed in the literature following extensions to Darcy's law proposed by Ergun (1952) or Forchheimer (1901). Generally, the extension consists in correcting the linear relation between the pressure gradient and the filtration velocity with a new term which takes into account the supplementary resistance due to inertial flows. This term scales as the filtration velocity magnitude raised to the power of n, where $2 \leq n \leq 3$. The more general model was obtained from upscaling techniques. Lasseux et al. (2008) used the volume-averaging technique to upscale the Navier-Stokes equations that govern two-phase flows at pore-scale. The authors extended the previous works on macroscopic creeping two-phase flows in homogeneous (Marle, 1982; Whitaker, 1986; Auriault and Sanchez-Palencia, 1986; Lasseux et al., 1996) and heterogeneous porous media (Quintard and Whitaker, 1988), and derived macroscopic equations for homogeneous media taking inertia effects into account. The complete model, not recalled here, involved primary and coupling multiphase permeability tensors, as well as primary and coupling inertia correction tensors.

Clavier et al. (2017) recently conducted column two-phase flow experiments and proposed constitutive relations for each relative permeability and inertia correction term. As pointed out in Davit and Quintard (2019), determining all the terms is very difficult and is still largely an ongoing work. In this study, we found low irreducible saturation in water, partly because of the very low interfacial tension between the chosen fluids. By considering the traditional curves for coupling permeabilities (Bacri et al., 1990; Rothman, 1990; Dullien and Dong, 1996), we estimated that coupling between the fluids is negligible because these are significant only for intermediate to high saturation in wetting fluid ($0.7 \lesssim S_w$). Consequently, we used a simpler model that does not take into account coupling permeabilities and coupling inertia correction.

Furthermore, we assumed that the model apparent permeability obeys a simple form, namely the extension of the well known Ergun's law (Ergun, 1952) for two-phase flows (Fourar et al., 2001). Consequently, continuity and momentum transport equations read

$$\nabla \cdot \mathbf{V}_i = 0 \quad i = w, n, \tag{1}$$

$$\nabla P_i = -\mathbf{V}_i \left(\frac{\mu_i}{K_0 k_{ri}} + \frac{\rho_i}{\eta \eta_{ri}} \|\mathbf{V}_i\| \right) + \rho_i \mathbf{g} \quad i = w, n, \tag{2}$$

where k_{ri} and η_{ri} are the relative permeability and passability of phase i, respectively, and η is the passability. We considered a homogeneous isotropic porous medium, that allows us to write the primary multiphase permeability as the product between a scalar relative permeability and a scalar absolute permeability K_0 (Bear et al., 1987; Quintard and Whitaker, 1988). Lipinski (1982), Schulenberg and Müller (1987) and Hu and Theofanous (1991), among others, have proposed correlations for relative permeabilities and relative passability, which depend on saturation and porosity. Ergun's correlation (Ergun, 1952) for η is used in this work and reads

$$\eta = \frac{\phi^3 d_b}{1.75(1-\phi)}. \tag{3}$$

We non-dimensionalized Eq. 2 with the following,

$$\mathbf{x} = L\mathbf{x}^\star,\ \mathbf{V} = U\mathbf{V}^\star,\ t = t^\star(L/U),\ P = P^\star\frac{\mu_n U L}{K_0}, \tag{4}$$

where the star exponent indicates dimensionless quantities. L and U are characteristic length and filtration velocity, respectively. The dimensionless equation, considering homogeneous and isotropic media, reads

$$\nabla^\star P_i^\star = -\mathbf{V}_i^\star\left(\frac{r_{\mu i}}{k_{ri}} + r_{\rho i}F_{oi}\|\mathbf{V}_i^\star\|\right) + r_{\rho i}G_r\mathbf{e}_z, \quad i = w, n, \tag{5}$$

where

$$G_r = \frac{\rho_n g K_0}{\mu_n U}, \tag{6}$$

is the gravity number, which compares the effect of gravity forces to the effect of the viscous forces at macroscopic scale,

$$F_{oi} = \frac{\rho_n U K_0}{\mu_n \eta_{ri}\eta} \quad i = w, n, \tag{7}$$

is the Forchheimer number (Ruth and Ma, 1992) for fluid i, which indicates the onset of significant macroscopic inertia effects (Ma and Ruth, 1993), and

$$r_\mu = \mu_w/\mu_n, \quad r_\rho = \rho_w/\rho_n, \tag{8}$$

are the viscosity and the density ratios, respectively.

2.2. Flow stability

Front displacement instabilities, by favoring the creation of preferential flow paths, also called fingers, make it very difficult to model the migration of a DNAPL (NAPL denser than water) from a source zone with Eqs. **??**-**??**. We commonly refer to the different instabilities as gravity, viscous or capillary fingerings, depending on the value of the dimensionless numbers and ratios of fluids viscosity and density (Saffman and Taylor, 1958; Lenormand et al., 1988). For DNAPL, gravity fingering has received a lot of attention (Schwille and Pankow, 1988; Glass and Nicholl, 1996; Nsir et al., 2012). Because the DNAPL is denser than water, its infiltration into an aquifer may lead to gravity fingering, depending on the magnitude and direction of DNAPL velocity. Among solutions to reproduce gravity fingering, Cueto-Felgueroso and Juanes (2009) introduced an additional fourth-order derivative of saturation in terms of the spatial coordinates. Saffman and Taylor (1958) and Chuoke et al. (1959) conducted a linear-stability analysis for a sharp invading front between two immiscible fluids in the absence of capillary forces. They gave a criterion for stability, which expresses the interplay between viscous and gravity forces. The Saffman-Taylor/Chuoke criterion is expressed in terms of V_c, the critical velocity of the fluid front between the invading fluid (in) and the displaced fluid (d),

$$|V_c| = \frac{\cos(\beta)\,(\rho_{in} - \rho_d)\,gK_0}{\phi(\mu_{in} - \mu_d)}, \tag{9}$$

where β is the angle formed by the gravitational vector and the direction of the flow. Tab. 2 lists the different stability scenarios. Among these scenarios, the intrusion of a DNAPL more viscous than water into a water-saturated soil is either conditionally stable for a downward flow or unconditionally stable for an upward flow. In practice, downward flows are observed when the DNAPL freely migrates from a source zone above the water table, whereas upward flows are observed in case of pressurized pipe ruptures below the water table, DNAPL pumping or groundwater upwelling. We only deal with stable flows in the following.

Table 2: Stability of two-phase flows, adapted from Glass and Nicholl (1996). V is the velocity of the invading front between the invading *in* and the displaced d fluids. The critical velocity may be either negative (downward flow) or positive (upward flow).

V_c	Conditionally stable		Unconditionally unstable	Unconditionally stable
< 0	$\mu_{in} < \mu_d$, $\rho_{in} < \rho_d$	$\mu_{in} > \mu_d$, $\rho_{in} > \rho_d$	$\mu_{in} < \mu_d$, $\rho_{in} > \rho_d$	$\mu_{in} > \mu_d$, $\rho_{in} < \rho_d$
	$\lvert V \rvert < \lvert V_c \rvert$	$\lvert V \rvert > \lvert V_c \rvert$		
> 0	$\mu_{in} < \mu_d$, $\rho_{in} > \rho_d$	$\mu_{in} > \mu_d$, $\rho_{in} < \rho_d$	$\mu_{in} < \mu_d$, $\rho_{in} < \rho_d$	$\mu_{in} > \mu_d$, $\rho_{in} > \rho_d$
	$\lvert V \rvert < \lvert V_c \rvert$	$\lvert V \rvert > \lvert V_c \rvert$		

3. Experimental method

The experimental setup and protocols were designed to produce a stable displacement with an upward flow of DNAPL in a porous medium saturated with the wetting fluid. The complete laboratory-scale (decimetric) setup is described below and shown in Fig. 1.

3.1. 2D tank and pumping system

The porous medium was embedded in the main reservoir of a tank made in polyvinylidene fluoride (PVDF). Two counter-channels positioned on both lateral sides allowed to keep the pressure head constant. These counter-channels were separated from the main reservoir by thin perforated metal grids. The front part of the tank was made of glass in order to monitor the two-phase displacement with photography. However, the back part was made with PVDF to allow inserting a network of Time-Domain Reflectometer (TDR) sensors (Decagon Devices 5TE 40567). The dimensions of the main reservoir were: 50 cm long, 30 cm high and 7 cm thick. Five nozzles of diameter 3.125 cm, at the bottom of the tank, allowed the connection of tubes to inject the fluids. Given the tank depth and the size of the inlet, small 3D effects near the nozzle may occur, but Philippe et al. (2021) have shown that this effect remained negligible using the same apparatus and fluids.

The injection system consisted of two peristaltic pumps (Watson Marlow 530U). One was dedicated to the injection of the oil by a bottom nozzle while the other was connected to the two lateral tank reservoirs and maintained a constant level of ethanol during the injection. During the injection, the in-

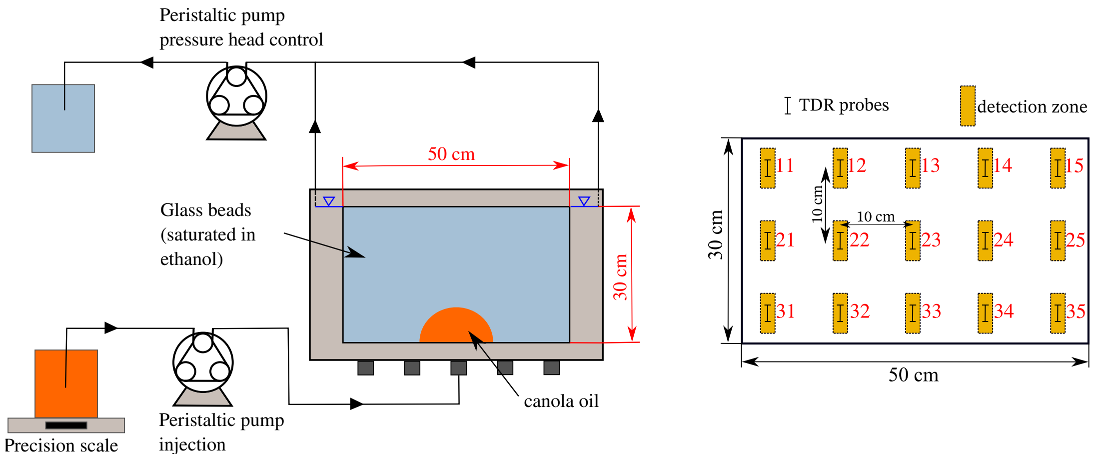

Figure 1: Left: schematic front view of the experimental 2D tank setup. One peristaltic pump is connected to the two lateral tank reservoirs and controls the pressure head, while a second pump injects the DNAPL in the main reservoir. This reservoir was filled with glass beads and initially saturated in wetting fluid. The precision scale recorded the injected mass of DNAPL. Right: arrangement of the 3×5 TDR probes in the main reservoir. The labeling is done following the row/column indice. The orange zone represents the detection area of the probes.

vading fluid was pumped from a beaker placed on a precision scale (Sartorius Cubis MSE $\pm$ 0.1 g). The mass of fluid injected was recorded every 300 ms and the inlet flow rate was calculated accordingly. Fig. 1 shows a sketch of the complete pumping setup.

3.2. Porous media and fluids

The unconsolidated porous medium was a packing of homogeneous glass beads of diameter d_b. We conducted diferrent experiments using either 1 mm or 2 mm diameter glass beads to study the impact of permeability and gravity forces during the injection. We measured the same porosity for each diameter ($\phi \approx 0.4$), and $K_0 = 3.5 \times 10^{-10}\,\mathrm{m}^2$ and $K_0 = 4.2 \times 10^{-9}\,\mathrm{m}^2$ for the

Table 3: Dynamic viscosity, density, surface tension and contact angle of the canola oil and ethanol used in the experiments (20°C) (Philippe et al., 2020). Viscosity ratio is $\mu_o/\mu_e = 61$ and density ratio is $\rho_o/\rho_e = 1.12$.

Properties	Canola oil (o)	Ethanol (e)
μ (Pa s)	1.18×10^{-1}	1.93×10^{-3}
ρ (kg/m^3)	911	808
$\sigma_{o/e}$ (N/m)	2.2×10^{-3}	
$\theta_{o/e}$	127°	

absolute permeability of the 1 mm and 2 mm glass beads, respectively.

We used ethanol 95% as the wetting invaded fluid and canola oil as the non-wetting invading fluid. We selected this fluid pair because the ratio between the different fluid properties is very close to a coal tar-water pair (Philippe et al., 2020). On the other hand, these fluids are non-toxic unlike the initial coal tar, which eased manipulation. Dynamic viscosity, density, surface tension, and contact angle at 20°C are given in Table. 3. The canola oil stood for the DNAPL, compared to ethanol, and the viscosity ratio ensured an unconditionally stable displacement. These two fluids have very low solubility (Rao and Arnold, 1956), which allowed precise identification of the fluid front, considering the time scale of the experiments (less than 20 minutes at a controlled temperature room of around 20°C).

3.3. Monitoring system

The monitoring of the fluid front was made in two ways:

1. By acquiring the averaged saturation around TDR probes that are disposed as an array of 3 × 5 probes. We show in Fig. 1 (right) the

arrangement of the probes and their labeling, following a row/column identification (tdr$_{ij}$ refers to the row i/column j probe). The TDR probes measured the averaged relative permittivity in the area close (up to 2 mm away) to the probes. The measured averaged relative permittivity $\bar{\varepsilon}$, acquired every 30 s, corresponds to the relative permittivity of the mixture of the three phases. The saturation in ethanol was then obtained through the permittivity ε_o of the mixture {glass beads + oil} and ε_e for the mixture {glass beads + ethanol}, then considering a linear relationship between these two endpoints,

$$S_w = \frac{\bar{\varepsilon} - \varepsilon_o}{\varepsilon_e - \varepsilon_o}, \tag{10}$$

where ε_e and ε_o are specific to each TDR probe and for each diameter of glass beads. We suggested a linear relationship because the difference between the two endpoints (porous media saturated with oil or ethanol) relative permittivity is small ($\varepsilon_e \simeq 6$ and $\varepsilon_o \simeq 14$) and that it gives a good approximation of the commonly used power law model (Complex Refractive Index Model, CRIM) (Birchak et al., 1974). This last has been proved to be accurate for a DNAPL/mineral/water mixture (Ajo-Franklin et al., 2004; Colombano et al., 2021a).

2. By acquiring the fluid front after post-processing the photos. We used a digital camera Nikon D810 with NIKKOR LENS 105, and a setup including two floodlights and black and white reflectors, to avoid any reflections and to optimize the contrast. To obtain a homogeneous lighting, experiments were performed in a dark room and the only source of light came from the two floodlights. Photos were taken each 30 s as soon as the injection tube was filled with oil. All photos were acquired

in RAW Nikon format (.nef). The post-processing was made with ImageJ, an open-source image processing program (Schneider et al., 2012). The process of going from raw photos to the interface is as follows. We first converted the raw photos to .tiff format with RawTherapee software and then to 8-bit format with ImageJ. A gray scale on the side of the tank ensures that the min and max values are set correctly for linear scaling to 256 shades of gray. Next, a px to cm conversion scale was provided to ImageJ based on the graduations on each side of the tank. The position of the interface was finally determined manually using the difference in shades of gray, as was done in (**?**), and recorded as the 2D coordinates of a set of points.

3.4. Experimental protocols

Fig. 2 shows the flowchart of the experimental protocols. The first one involved performing several injections of canola oil from the center bottom hole in glass beads (d_b=1 and 2 mm) fully saturated with ethanol (as schematized in Fig. 1). The flow rate was also changed for glass beads d_b=1 mm. Another experiment, performed with d_b=2 mm, consisted in injecting the oil in the same way as before but in glass beads with an initial field of residual oil saturation. Starting from glass beads saturated with ethanol, the residual oil saturation was created by performing a prior drainage, followed by a final imbibition.

For each experiments, a volume of glass beads of very small diameter (0.1 mm) was poured to fill the dead volume between the bottom of the tank and the top of the injection nozzle (about 1.5 cm) to prevent the flow of DNAPL below the injection point. Then, the packing was made by pouring

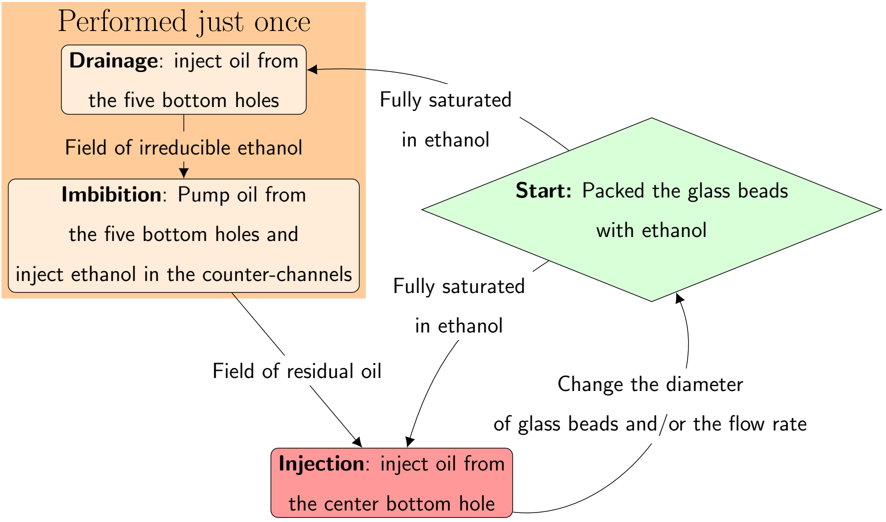

Figure 2: Flowchart of the protocols used in this study. One experiment was dedicated to injecting the oil in the glass beads with an initial residual saturation in oil. The other experiments involved injecting the oil in a fully saturated porous media for different size of glass bead and flow rate.

in several times a layer of beads into a volume of ethanol to obtain a more homogeneous packing.

4. Numerical method

The experimental results showed that the displacement front is sharp. Generalized Darcy's laws produce diffusive fronts, although shocks may be obtained if there is no capillary pressure and the diffusive front is due to mobility non-linearity. Effective properties in generalized Darcy's law may be tweaked to obtain a diffuse interface method as shown in **??**. However, given the fact that the geometry remains very simple, experimental results suggest that a more direct Lagrangian method may be more effective. We therefore adopted an Arbitrary Lagrangian-Eulerian method (ALE), which is described in the next section along with its implementation. For comparison we have also reproduced the experimental results with the generalized Darcy model.

4.1. Equations

ALE methods are commonly used to track interfaces between deforming domains, for example in fluid-structure interaction problems (Hu et al., 2001). The geometry and the mesh can change, given a set of constraints. In our case, the interface between the two fluid domains was deformed under the computed Darcy-velocity field and the displacement of the mesh nodes was computed using Laplace's equation

$$\nabla^2 \mathbf{X} = 0, \tag{11}$$

where $\mathbf{X}$ are the cartesian coordinates of the material frame. The differential operator is defined in respect to the Cartesian coordinates of the spatial frame.

We solved the continuity equation and a single-phase Darcy's law with Forchheimer correction. For a homogeneous isotropic medium, the equations read

$$\nabla \cdot \mathbf{V} = 0, \quad \nabla P = -\mathbf{V} \left(\frac{\mu_i}{K_0} + \rho_i \eta^{-1} \|\mathbf{V}\| \right) + \rho_i g \mathbf{e}_z, \tag{12}$$

where the material properties μ and ρ are attached to a domain (fluid) and η is the passability, which depends only on the porous medium. As pointed out in the recent review in Davit and Quintard (2019), equation 12 has limitations. For instance, it does not take into account anisotropy for the inertia corrections (see e.g. Lasseux et al. (2011)). The quadratic correction is also only an approximation and other inertia regimes exist (Mei and Auriault, 1991; Wodie and Levy, 1991; Firdaouss et al., 1997; Lasseux et al., 2011). However, Ergun's equation 12 remains a simple and widely used model that takes into account the additional drag from inertia with good accuracy.

These equations were solved using a finite element approach with a polynomial (quadratic) interpolation function for the pressure and time stepping was governed by an implicit Backward Differentiation Formula (BDF) method. The whole numerical model was solved using Comsol Multiphysics®.

We also solved the generalized Darcy equations to compare with the experimental results. The model reads

$$\phi \frac{\partial S_i}{\partial t} + \nabla \cdot \mathbf{V}_i = 0, \tag{13a}$$

$$\mathbf{V}_i = -\frac{k_{ri}(S_w, ...)\mathbf{K}_0}{\mu_i} \cdot \left(\nabla P_i - \rho_i g \mathbf{e}_z\right), \tag{13b}$$

$$S_w + S_n = 1, \tag{13c}$$

$$P_w = P_n. \tag{13d}$$

Introducing Eq. 13b into Eq. 13a and using Eq. 13c and Eq. 13d, we eliminate two unknowns and choose as primary variables the pressure of the non-wetting fluid and the wetting fluid saturation. We obtain the following non-linear parabolic system,

$$\phi \frac{\partial S_w}{\partial t} = \nabla \cdot \left[-\frac{k_{rw}(S_w)\mathbf{K}_0}{\mu_w} \cdot \left(\nabla P_n - \rho_w g \mathbf{e}_z\right) \right], \tag{14a}$$

$$\phi \frac{\partial (1 - S_w)}{\partial t} = \nabla \cdot \left[-\frac{k_{rn}(S_w)\mathbf{K}_0}{\mu_n} \cdot \left(\nabla P_n - \rho_n g \mathbf{e}_z\right) \right], \tag{14b}$$

which is the starting point to solve two-phase flows in different multiphase flow solvers at Darcy-scale (Flemisch et al., 2011; Horgue et al., 2015). Here, we used the OpenFoam toolbox developed by Horgue et al. (2015), in which an IMPES algorithm is adopted. We used van Genuchten relations (Van Genuchten, 1980) for the relative permeabilities. The appropriate coefficients for the pair of liquids used in this study in 1 mm glass beads were measured by Philippe et al. (2020). To be consistent with the experimental observations and ALE modeling, we neglected the capillary pressure as well as the coupling relative permeabilities.

4.2. Geometry and boundary conditions

Fig. 3 shows the geometry used in the numerical study. A pressure head condition was set on the left/right boundaries (pressure of ethanol). A null flux was set on the bottom boundary (i.e., the top of the layer of 0.1 mm glass beads), except at the inlet, where a given flux is imposed following the measured $U_{2D}(t)$ obtained previously. We also used a pressure condition at the inlet to model a pumping scenario, more suitable to emphasize the impact of inertia upon the shape of the oil front in that case. As the interface was handled explicitly, we imposed a boundary condition, derived in Appendix A, which reads

$$\mathbf{w} \cdot \mathbf{n} = \frac{1}{\phi(1 - S_{ei} - S_{or})} \mathbf{V} \cdot \mathbf{n}, \tag{15}$$

where $\mathbf{w}$ is the velocity of the interface, $\mathbf{n}$ the normal vector at the interface, and S_{ei} and S_{or} are those obtained from the TDR probes (Tab. 6). The initial fluid configuration was a half-ellipse corresponding to the interface measured at the initial time (2 min after the beginning of the injection) of each experiment.

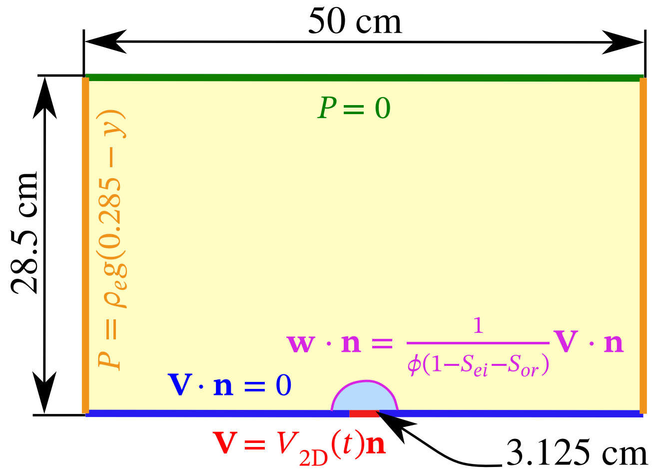

Figure 3: Geometry and label of the boundaries. Dirichlet conditions were set on the left and right boundaries (pressure head), and the top boundary (reference pressure). Neumann conditions were set on the inlet boundary (from the relation $U_{2D}(t)$) and on the bottom boundary (null flux). The condition at the fluid front depends on the Darcy-velocity field.

4.3. Mesh sensitivity analysis

The mesh sensitivity analysis is based on the position of the interface between the two fluids after 11 min of injection. The inlet velocity is constant in time, the residual and irreducible saturation are zero and the porosity is the same as for the actual porous media ($\phi = 0.4$). The absolute permeability is $K_0 = 5 \times 10^{-9}\,\mathrm{m}^2$ to test the mesh convergence with non-negligible gravity forces. An automatic remeshing procedure allowed us to keep the global mesh quality higher than a given threshold, which is mandatory to avoid element degeneration. Fig. 4 shows the position of the front at the final time for three different mesh sizes. The position of the front was identical regardless of the number of mesh elements. We chose the finest mesh, as computational time is low even for the finest mesh.

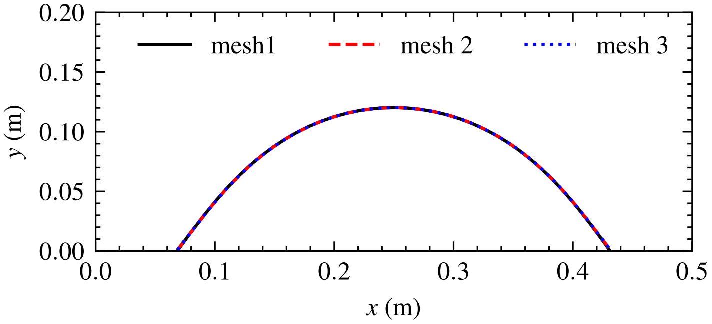

Figure 4: Comparison of the position of the interface for three different meshes. Mesh 1, 2, and 3 are made of 2,150, 23,600, and 52,400 free triangular mesh elements, respectively.

5. Experimental results: laboratory-scale injections

We first analyze the data from the precision scale, from which we can derive the inlet flow rate. From the flow rate and the fluid and porous media properties, we calculate the dimensionless numbers that characterized the two-phase displacements. Finally, post-processing of TDR data and photos allow us to characterize the two-phase displacement, providingd insight regarding which model is suitable to reproduced the experiments.

5.1. Mass balance analysis

We injected between 18% and 32% of the pore volume after twelve minutes of injection (based on porosity $\phi = 0.4$), depending on the flow rate. Two injections in 2 mm and 1 mm glass beads were similar, whereas a second injection in 1 mm was conducted with a higher flow rate. In the following, we refer to these 1 mm experiments as 1 mm Q_l and 1 mm Q_h, respectively.

The corresponding 2D velocity was calculated based on the flow rate, the tank's depth and the diameter of the inlet hole. Fig. 5 shows the 2D velocity as a function of time. We obtained the relation $V_{2D}(t)$ by linear regression over the time interval 120 s to 690 s. These relations were used for the numerical modeling. V_{2D} slightly decreased with the injection time, and the difference in injection velocity between 1 mm Q_h and 1 mm Q_l experiments was about 15%. The decreasing trend can be imputed to the increasing pressure head, as ethanol was replaced by oil, which is denser. The y-intercept values V_{2D} were used to compute the relevant pore-scale and Darcy-scale dimensionless numbers.

Pore-scale and Darcy-scale dimensionless numbers for each experiment are listed in Tab. 5. Reynolds and capillary numbers were about the same order of magnitude for each experiment and sufficiently low for considering that the hypothesis of creeping flow with a low capillary number at pore-scale was fulfilled. On the other hand, Bond number is up to 1.8 for 2 mm experiments, so within the limits of the assumptions underlying the continuous macroscale model used in the following. An order of magnitude separates the gravity numbers for the 1 mm and 2 mm experiments, suggesting different large-scale dynamics between these experiments. The Forchheimer number was very low for each experiment, which suggests negligible macroscopic inertia effects in our experiments. This is confirmed with previous studies that found a negligible error on the pressure drop when calculated with Darcy's law for Forchheimer numbers below 10^{-1} (Zeng and Grigg, 2006; Macini et al., 2011).

5.2. TDR analysis

TDR probes were used to study the dynamic of the injection but also to obtain the irreducible saturation in ethanol S_{ei} and the residual saturation in

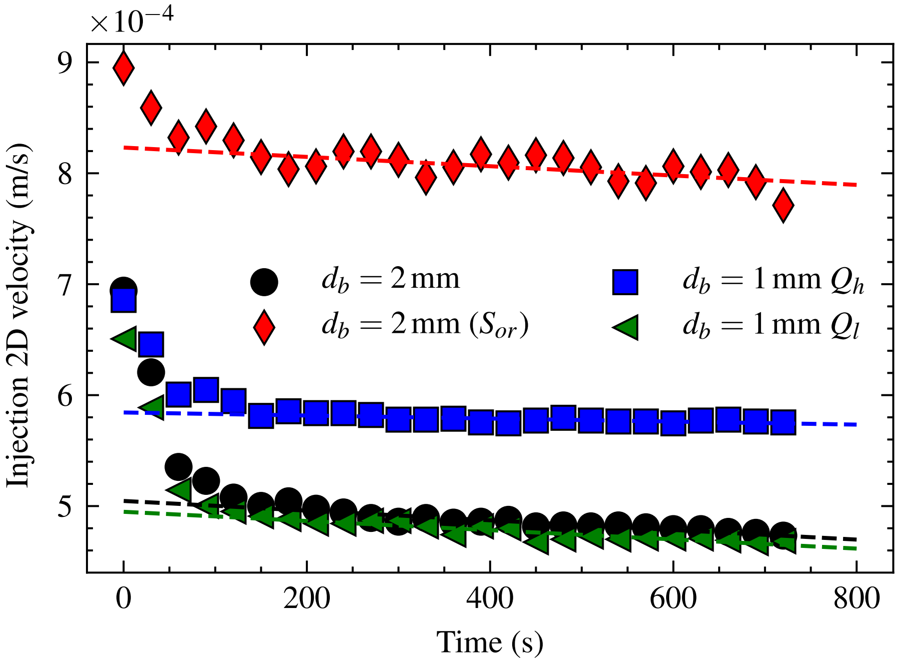

Figure 5: Injection 2D velocity V_{2D} as a function of time for each experiment. V_{2D} was calculated by dividing the injection flow rate by the tank's depth and the diameter of the inlet hole. The relations $V_{2D}(t)$ were obtained by linear regression over the time interval 120 s to 690 s, and were used as a boundary condition for the numerical model. The y-intercept value was used to calculate dimensionless numbers.

Table 4: Pore-scale dimensionless numbers for each experiment.

Experiment	$Re = \frac{V_{2D}\rho_o d_b}{\phi\mu_o}$	$Ca = \frac{V_{2D}\mu_o}{\phi\sigma}$	$Bo = \frac{\Delta\rho g d_b^2}{\sigma}$
2 mm	1.9×10^{-2}	2.7×10^{-2}	1.8
2 mm S_{or}	3.2×10^{-2}	4.4×10^{-2}	1.8
1 mm Q_h	0.9×10^{-2}	3.1×10^{-2}	0.4
1 mm Q_l	1.1×10^{-2}	2.6×10^{-2}	0.4

Table 5: Darcy-scale dimensionless numbers, as defined as in Eqs. 6-7, for each experiment. Here, $\eta_{ri} = 1$ in fluid i.

Experiment	G_r	F_o
2 mm	31.5×10^{-2}	6.7×10^{-5}
2 mm S_{or}	19.3×10^{-2}	10.9×10^{-5}
1 mm Q_h	4.5×10^{-2}	2.6×10^{-5}
1 mm Q_l	5.3×10^{-2}	2.2×10^{-5}

oil S_{or}. The irreducible saturation and the residual oil saturation were used for the modeling part. Fig. 6 shows the saturation given by the three TDR probes 32 to 34 (middle columns, lower row, see Fig. 1) for each experiment. Based on probes 32 and 34, we see that the evolution of the front was symmetrical on each side of the injection point, except for the injection in the 1mm Q_h glass beads for which the right side was slightly ahead.

Irreducible ethanol saturation and residual oil saturation were obtained by averaging the results from probes 32 to 34 at the final time. Tab. 6 summarizes all the results. We measured a lower irreducible saturation for a lower flow rate. The difference is noticeable, between 12% and 6%, for 1mm Q_h and 1mm Q_l, respectively, although the difference in inlet flow rate remained moderate for these two injections. For the same flow rate, the irreducible saturation was higher in the more permeable medium (2 mm beads). However, the small number of values and the dispersion between these values does not allow to be categorical on this point. Finally, we found that the irreducible ethanol saturation is lower for the experiment with 2 mm glass beads with an initial residual oil saturation (about 22% of residual oil)

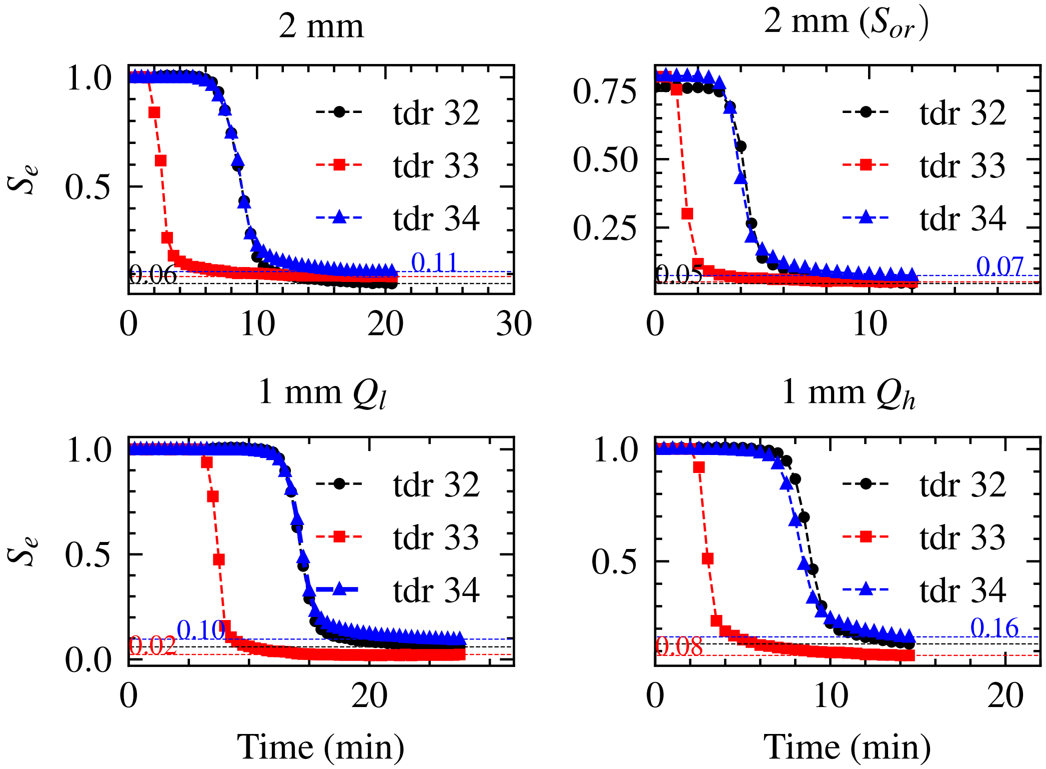

Figure 6: Evolution of the saturation given by the three TDR (center columns/bottom row). The final value indicates the irreducible ethanol saturation in the oil zone.

Table 6: Estimation of the irreducible saturation in ethanol for the different experiments. Results obtained from the means of the three TDR probes (32-33-34).

Experiment	S_{ei}	S_{or}
2 mm	8.7% ± 2.0%	-
2 mm (S_{or})	5.6% ± 0.9%	22.3% ± 2.0%
1 mm Q_h	12.3% ± 3.3%	-
1 mm Q_l	6.0% ± 3.2%	-

compared to the fully saturated case, despite the higher flow rate.

5.3. Photos analysis

From the photos[1] (see Fig. 7a and Fig. 7b showing as an example the injected oil after 7 minutes, in 2 mm and 1 mm Q_l glass beads, respectively), we observed a flattened half-disk shape of the oil zone for 2 mm glass beads. This shape is due to the impact of gravitational forces on the injection process. In contrast, the shape of the oil zone looks like a half-disk in the case of injection in 1 mm glass beads (at both flow rates).

We also observed that the fluid front was very well-defined and sharp for each injection. The front spanned only over a few glass beads at most, and the displacements were stable due to the fluid properties and the experimental protocol. Consequently, all injections can be modeled by the advance of a macroscopic front. This is an important feature, which allowed us to use a

---

[1] All the photos and the fluid front coordinates are available as supplementary material in the associated data repository: `https://data.mendeley.com/datasets/7njyhc65w6/draft?a=ef3a9a24-ae72-4260-bb3b-62a81b210329`

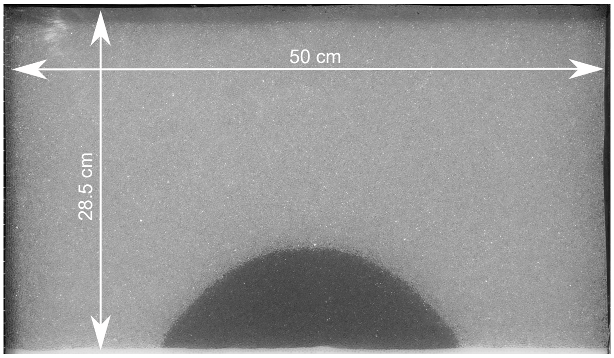

(a) Saturation field at the time $t = 7$ min for 2 mm injection.

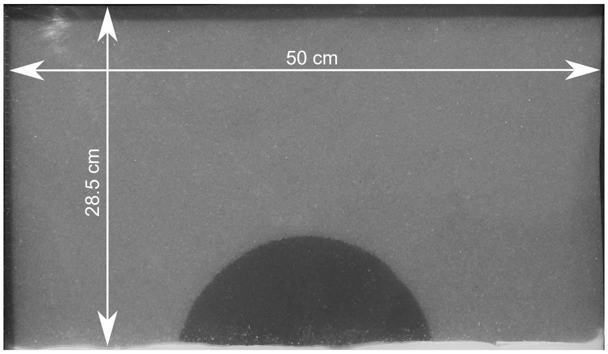

(b) Saturation field at the time $t = 7$ min for 1 mm Q_l injection.

Figure 7: Photos of oil saturation at the time $t = 7$ min. The thin layer of very low permeable beads (0.1 mm) allows to close the 1.5 cm space at the bottom of the tank so that the useful medium is at the level of the injection point.

numerical method that explicitly captures the front displacement. To this end, photo analysis was used to extract the fluid interface, as described in the method section, and compare them with the numerical model results.

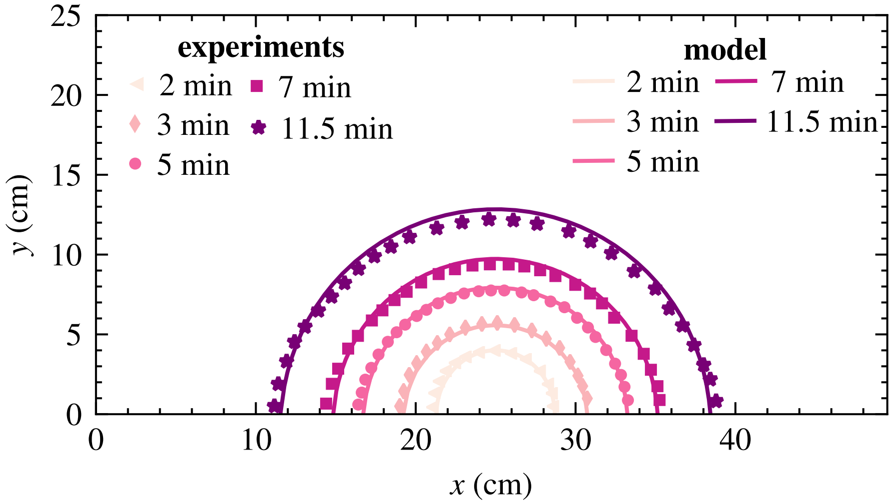

Figure 8: Comparison at various time of the position of the fluid front from numerical modeling (solid lines) and experimental measurements (markers). Results for injection in 1 mm Q_l glass beads. Here, $S_{ei} = 0.06$, $\eta = 0$, and $K_0 = 3.5 \times 10^{-10}$ m^2.

6. Numerical results: model validation

The ALE code was validated against the experimental injection in glass beads packing by reproducing the fluid front for different times and each experiment. Fig. 8 shows the numerical and experimental fluid fronts between 2 and 11.5 minutes for 1 mm (Q_l) experiment. Results for the other 1 mm experiment are analogous. The proposed model predicted well the experimental results for the whole injection. As for the experiments, we observed the evolution of a semi-circular front. This shape of interface confirms that the displacement is mainly dominated by viscous forces and with very little influence from gravity forces. We noticed a small discrepancy ($\approx 6\%$) at the top of the oil dome after 11.5 minutes of injection, where the numerical front was slightly in advance compared to the measured front.

Fig. 9a and Fig. 9b show the numerical and experimental fluid front for 2 mm experiments with and without initial residual oil saturation, respectively. Here again, the position of the fluid front during injection was well reproduced, in particular the flattening of the front and the lateral extension of the oil under the action of gravity. We noticed a larger discrepancy ($\approx 10\%$) between the model and experiments at the final time compared to 1 mm experiments. The numerical model predicted a less flattened oil zone than what we measured experimentally. This may have happened because of the uncertainty on the absolute permeability or a locally lower irreducible saturation in ethanol. Indeed, we measured the absolute permeability in a column apparatus so the packing may be different from the one in the tank.

Fig. 10 shows the saturation field from modeling and the experimental front as a black line. The top row shows experiment vs. modeling results in 1 mm Q_h glass beads at time 7 min and 11.5 min. The bottom row shows the same comparison for the experiment in 2 mm glass beads. In both cases, the position of the front is well reproduced, as well as the lateral spreading of the oil under gravity forces (experiments in 2 mm beads)

In conclusion, the proposed model can predict the evolution of the front in versatile situations (flow rate, irreducible and residual saturation) with good accuracy for 1 mm glass beads and 2 mm glass beads during the first part of the injection. However, it fails to accurately reproduce the position of the top of the oil front in the last part of the injection in 2 mm glass beads. As shown, the generalized Darcy equations also fails to reproduce precisely this part of the experimental results.

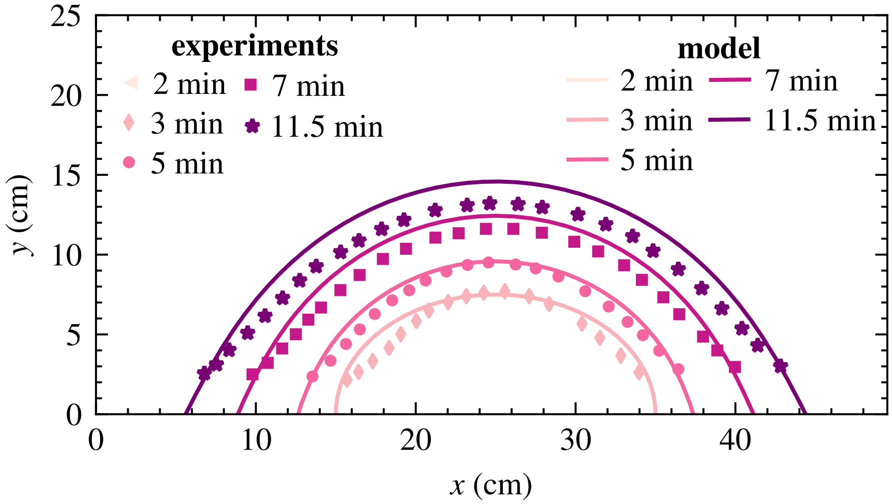

(a) Comparison for injection in 2 mm glass beads with initial residual saturation ($S_{ei} = 0.056$ and $S_{or} = 0.23$).

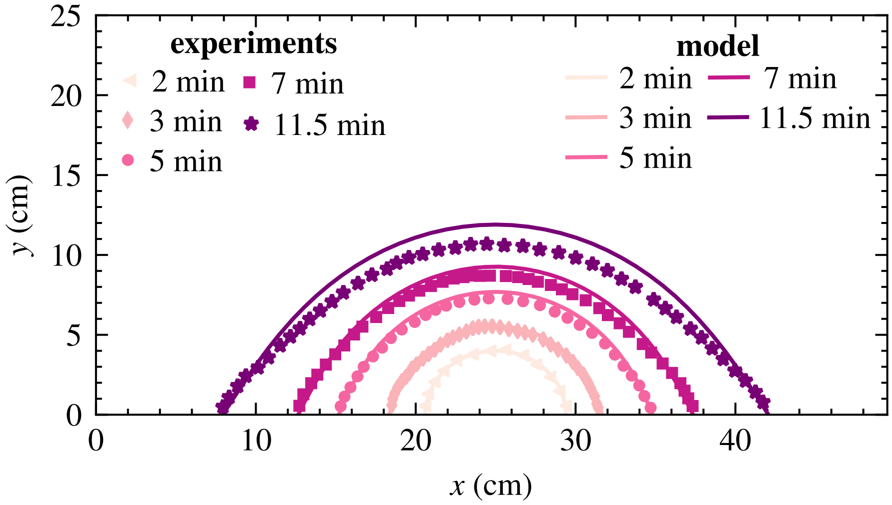

(b) Comparison for injection in 2 mm glass beads ($S_{ei} = 0.087$) .

Figure 9: Comparison at various time of the position of the fluid front from numerical modeling (solid lines) and experimental measurements (markers). Results for $\eta = 0$, and $K_0 = 4.2 \times 10^{-9}$ m^2.

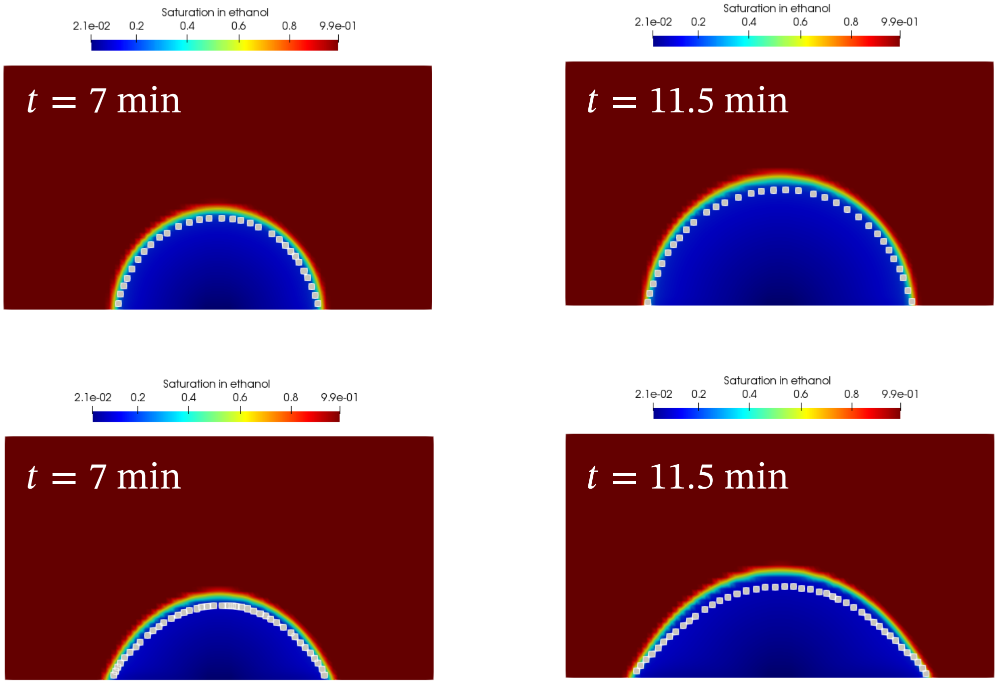

Figure 10: Comparison between experiments (black line) and modeling with generalized Darcy equations (field). Top row shows result for 1 mm Q_h glass beads and bottom row shows result for 2 mm glass beads experiment.

7. Numerical results: parametric study of pumping and injection scenarios

Comparison against the experimental injection in glass beads packing at different flow rate and different glas beads diameter have allowed us to validate our modeling approach but are very limited in scope. To understand further the impact of the displacement of DNAPL in highly permeable porous media, we investigated two different numerical cases: (i) an injection scenario similar to the experiments previously described, and (ii) a pumping scenario very close to the experiments conducted in Philippe et al. (2021). In the latter, the authors performed isothermal and non-isothermal pumping experiments in the same 2D tank used in our study. They also used the same apparatus and the same fluids. The major difference is that we considered a viscosity ratio $r_{\mu e} = 1$ to avoid viscous fingering. A schematic representation of both scenarios is given in Fig. 11. We used the same boundary and initial conditions as already presented for the validation step, except for a symmetry condition on the left boundary and an impermeable wall condition on the right boundary for the pumping scenario.

Tab. 7 lists the values of parameters for both scenarios. We considered that there was no residual oil saturation and used a default value of irreducible ethanol saturation $S_{ei} = 5\%$. The viscosity and density ratios, as well as the porosity, have the same values as for the experiments, except for the pumping scenario for which we used matching viscosity for both fluids. We investigated gravity number values between 0.02 and 2 (values for experiments were between 0.05 and 0.3) without inertia correction ($F_o = 0$). We also studied values of F_o between 0.02 and 2 for a fixed gravity number

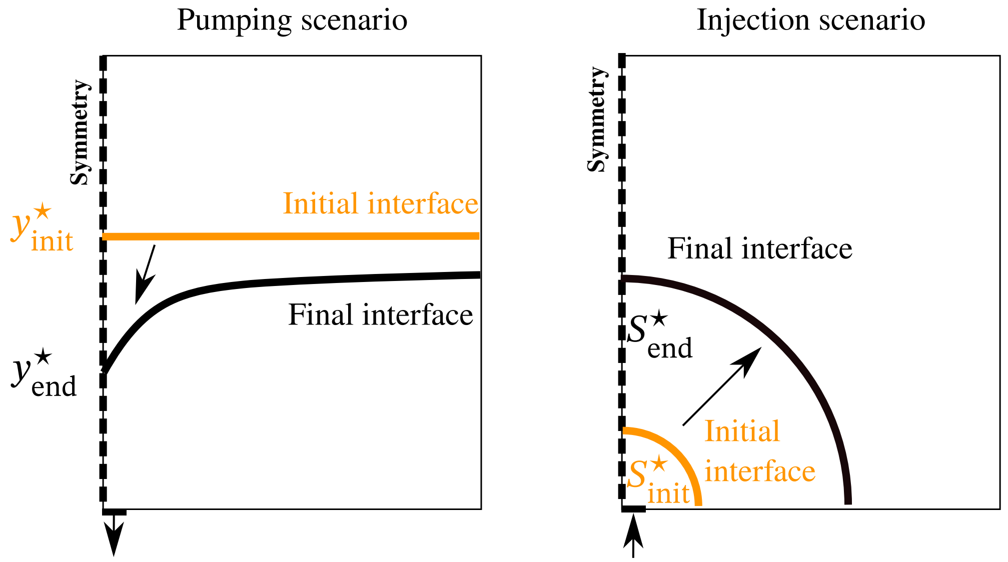

Figure 11: Schematics of the pumping (left) and injection (right) scenarios. $y^\star$ and $S^\star$ denote the dimensionless position along the y axis and the dimensionless surface occupied by the injected fluid, respectively. Only one half of the system was considered for the parameteric studies. The boundary conditions are the same as those used for the validation (Fig. 3), except for the symmetry boundary condition on the left and an impermeable wall condition on the right boundary for the pumping scenario.

Table 7: Parameters used, range of values and default values for both scenarios. Particular values for the pumping scenario are indicated with †.

Parameter	Lower bound	Upper bound	Default value
G_r	0.02	2	0.5
F_o	0.02	2	0
ϕ			0.4
$r_{\rho e}$	-	-	0.887
$r_{\mu e}$	-	-	$0.016 - 1^{\dagger}$
S_{ei}	-	-	0.05
S_{or}	-	-	0

($G_r = 0.5$) for both scenarios. The range used for the Forchheimer number in this parametric study is much broader than for the experiments (Tab. 5), for which inertia forces were negligible. The ranges of values chosen for these two parameters allowed us to study the influence of gravitational and inertial forces in very different situations, for example for low (G_r and F_o small) or highly permeable soils (F_o and G_r high). As an example, and assuming that the characteristic velocity and fluid properties are the same than for the experiments, the range value for G_r roughly corresponds to an absolute permeability between 100 and 10,000 darcy units.

7.1. Injection scenario

Fig. 12 shows the fluid front at the time $t^{\star} = 0.3$ for different values of the gravity numbers. We observed the same behavior as captured during the experiments, i.e., a perfect semi-circular front for low gravity numbers (viscosity-dominated displacement) and a flattened fluid front for a gravity

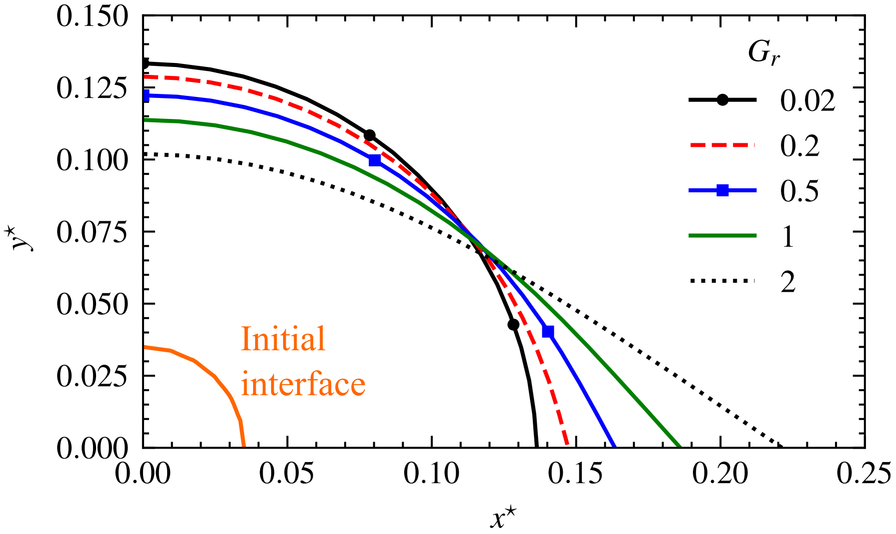

Figure 12: Fluid front at the dimensionless time $t^\star = 0.3$ for different gravity numbers (injection scenario). $x^\star$ and $y^\star$ denote the dimensionless length along the x and y axis, respectively.

number equal or higher than 0.2. Fig. 13 further shows the evolution of the eccentricity parameter as a function of the gravity number. We observed no critical gravity number for which the front starts to flatten, although the slope is not constant and the dependence upon the gravity number is not linear.

To investigate the impact of the Forchheimer number, we changed the inlet boundary condition from a constant inlet velocity to a constant pressure. The reason is that, when the velocity is imposed, we observed no significant change of the fluid front but rather a modification of the pressure drop, see Eq. 5). The inlet pressure, $P^\star = 0.15$, was chosen from the previous study on gravity numbers to be approximately equal to the pressure at the inlet when $G_r = 0.5$.

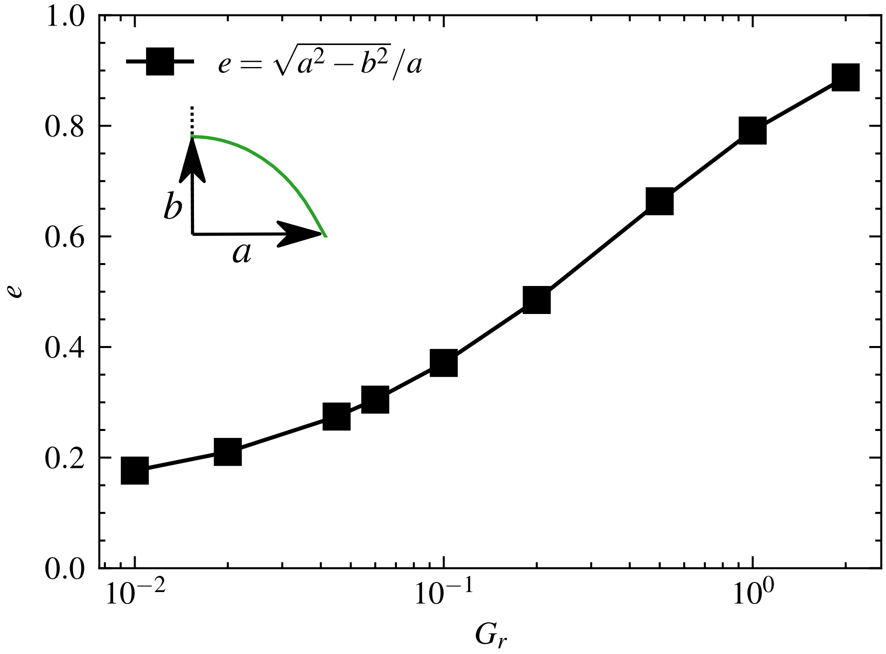

Figure 13: Eccentricity parameter characterizing the shape of the fluid front at the dimensionless time $t^{\star} = 0.3$ for different gravity numbers (injection scenario).

Fig. 14 shows the fluid front at time $t^\star = 0.3$ for different values of the Forchheimer numbers. The eccentricity parameter changes only slightly, rather the position changes with a slower front when the Forchheimer number increases due to the non-linear drag. Because of the inlet pressure condition, the injected volume at a given time evolves freely and is also determined by the drag. We plotted the surface occupied by the injected fluid at the time $t^\star = 0.3$ for different Forchheimer numbers (Fig. 15). The surface of injected fluid starts to significantly decrease for $0.1 \lesssim F_o$, with a change in behavior that is more pronounced than the previous study on the gravity number. A decrease in the surface of injected fluid corresponds to a lower Darcy-velocity, i.e., a non-negligible part of the pressure gradient is now overcoming the non-linear drag.

7.2. Pumping scenario

Fig. 16 shows the fluid front at $t^\star = 0.3$ for different values of the gravity numbers for the pumping scenario. The first observation is that larger gravity numbers correspond to a flatter front and to a longer time before the breakthrough. For $G_r = 2$, the fluid front is about 20% further from the pumping point than for $G_r = 0.02$, with respect to the initial distance.

Fig. 17 shows the fluid front at the time $t^\star = 0.3$ for different values of the Forchheimer numbers. As for the injection scenario, we changed the inlet boundary condition from a constant inlet velocity to a constant inlet pressure. This pressure was set to $P^\star = 10^{-2}$, which is low enough to pump the fluid when $G_r = 0.5$. The final volume of pumped fluid freely changes as a function of the supplementary drag due to inertia effects.

The breakthrough was almost reached for $F_o = 0.02$, for which the re-

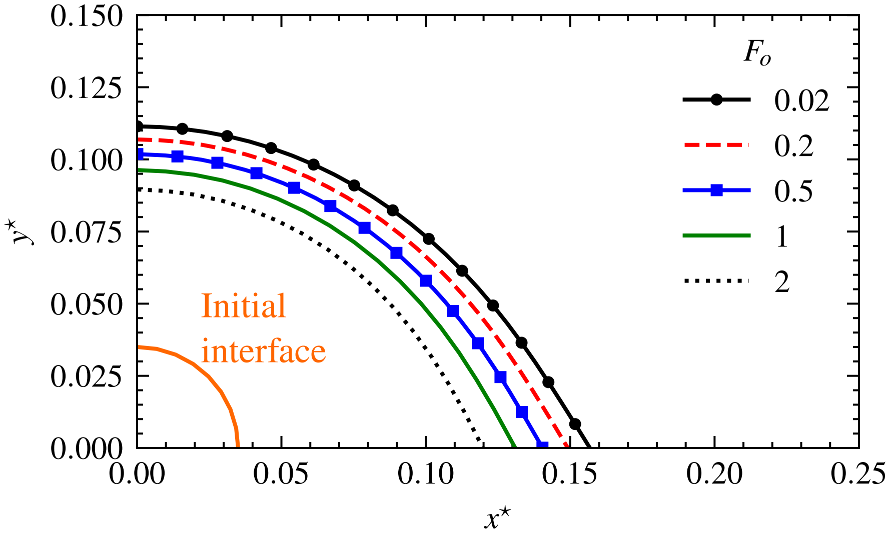

Figure 14: Fluid front at the dimensionless $t^\star = 0.3$ as a function of the Forchheimer number for the injection scenario. Results obtained for $G_r = 0.5$. $x^\star$ and $y^\star$ denote the dimensionless length along the x and y axis, respectively. The dimensionless inlet pressure is $P^\star = 0.15$.

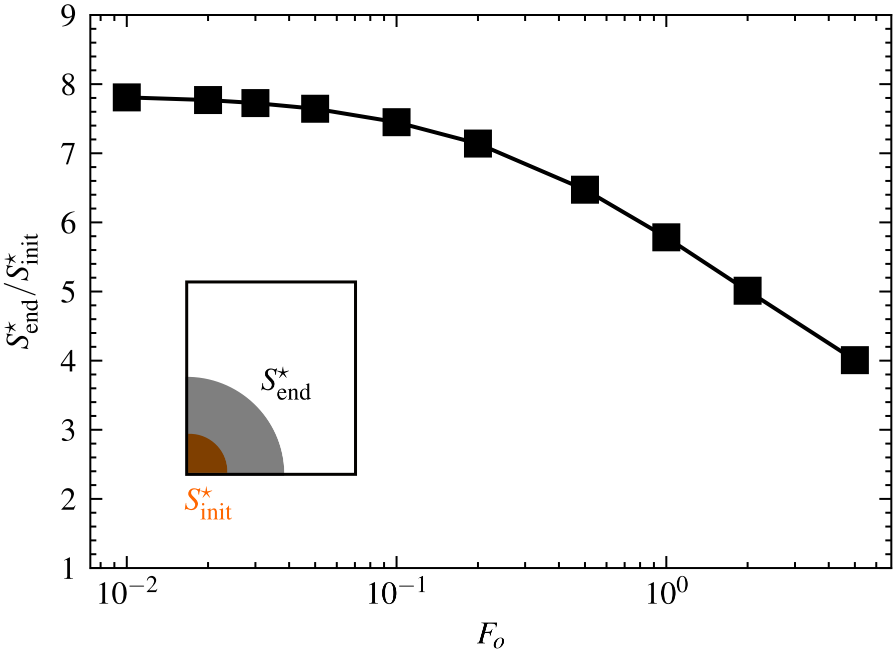

Figure 15: Dimensionless surface of injected fluid at the dimensionless time $t^\star = 0.3$ for different Forchheimer numbers (injection scenario). $S^\star$ denotes the dimensionless surface occupied by the injected fluid. Results obtained for $G_r = 0.5$. The dimensionless inlet pressure is $P^\star = 0.15$.

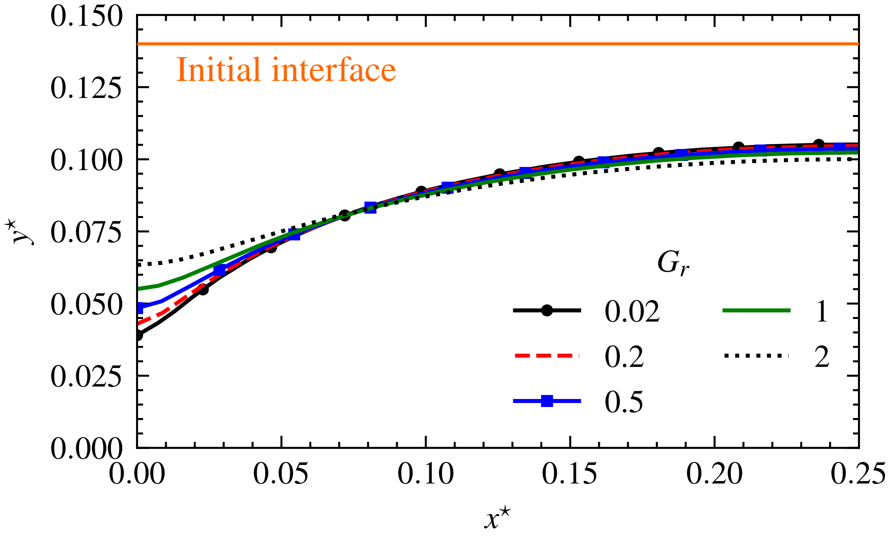

Figure 16: Fluid front at the dimensionless time $t^\star = 0.3$ for different gravity numbers (pumping scenario). $x^\star$ and $y^\star$ denote the dimensionless length along the x and y axis, respectively.

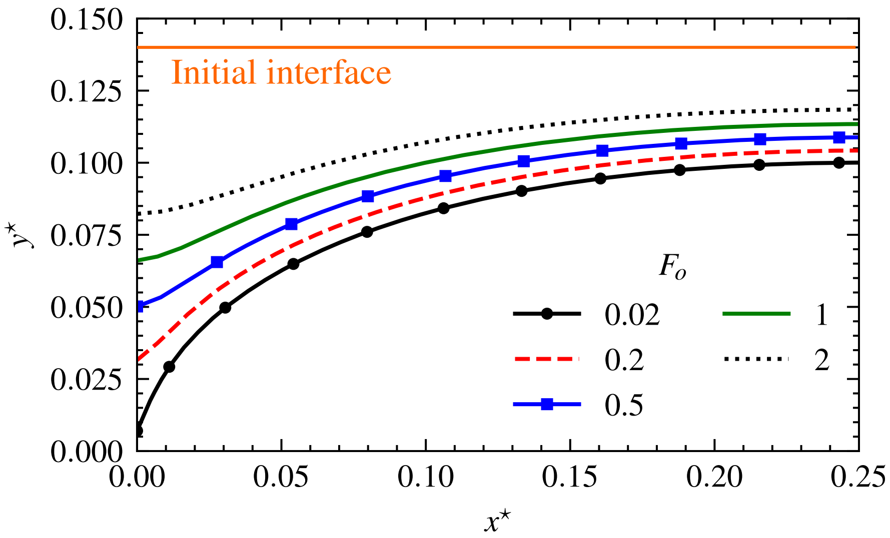

Figure 17: Fluid front at the dimensionless time $t^\star = 0.12$ for different Forchheimer numbers (pumping scenario). Results obtained for $G_r = 0.5$. $x^\star$ and $y^\star$ denote the dimensionless length along the x and y axis, respectively. The dimensionless inlet pressure was $P^\star = 10^{-2}$.

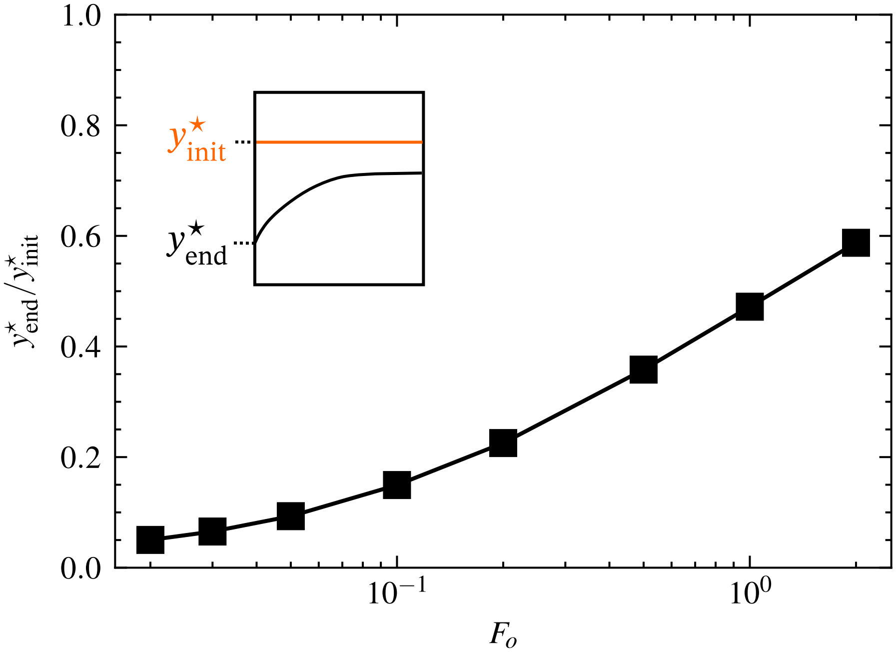

Figure 18: Distance between the fluid front and the pumping point for different Forchheimer numbers at the dimensionless time $t^\star = 0.12$ (pumping scenario). $y^\star$ denotes the dimensionless length along the y axis. Results obtained for $G_r = 0.5$.

sistance due to inertia is very small and the magnitude of the velocity field was higher. In contrast, when the resistance due to inertia was higher, much less fluid was pumped and the fluid front was about 55% further away from the pumping point for $F_o = 2$ than for the case of $F_o = 0.02$ (Fig. 18). The impact of inertia was significant for $0.1 \lesssim F_o$ (about 0.2 for the injection scenario) with a front that was at least 15% further away from the pumping point.

8. Discussion

Our results for different problem classes indicate that the impact of inertia and gravity on the fluid front are non-negligible. While we found no clear critical value, we observed a mild threshold value for inertia, with significant effects starting for $0.1 \lesssim F_o$. For gravity, the evolution is more progressive without a threshold value.

Gravity numbers between 10^{-1} and 1 are commonly encountered in two-phase flows in contaminant hydrology. For example, $G_r \approx 0.6$ for a contaminated site (chlorinated hydrocarbon, groundwater velocity 10 m/day, and permeability between 10^{-11} to 10^{-9} m^2) located in southeastern France (Omirbekov, 2020). The "DNAPL" and ethanol couple used in this work is similar to a coal tar/ water couple. Since coal tar is a highly viscous DNAPL ($\mu_o \approx 0.12$ Pa s), gravity numbers $G_r \approx 1$ were observed only for the most permeable media of 4,200 darcy units (2 mm glass beads). However, gravity effects may be non-negligible for lower and more standard permeabilities, since many DNAPLs are less viscous than the coal tar displacement we have mimicked here with a canola oil and ethanol couple, e.g., chlorinated solvents or elemental mercury.

Several works have discussed "threshold" values for F_o from which inertia effects may be considered non-negligible (remembering, as discussed above, that there is no such thing as a critical number). Zeng and Grigg (2006) found that for $F_o = 0.11$, 10% of the pressure drop is due to inertia effects. Macini et al. (2011) found the onset of non-negligible inertia effects for $0.22 < F_o < 0.56$ based on experiments in different sands for gas injection. Ghane et al. (2014) proposed a similar range of values ($0.14 < F_o < 0.55$) with water injection in denitrification beds. The threshold value for the Forchheimer number that we have found is therefore consistent with the literature.

Such values are harder to reach in contaminant hydrology and less common than large gravity numbers. Previous work focuses either on gas flows, which is much less viscous than DNAPL, at high pressure with superficial velocities as high as tens of cm/s in less permeable media (i.e. the passability is smaller) or on water flow in highly permeable media such as wood chips (up to $10^{-8}\,\mathrm{m}^2$). Considering a DNAPL used recently by Colombano et al. (2020) ($\mu_o = 5 \times 10^{-3}$ Pa s and $\rho_o = 1661\,\mathrm{kg\,m}^{-3}$), the superficial velocity required to reach the threshold value for Forchheimer number in 2 mm glass beads ($K_0 = 4200$ darcy units) is in the range of several cm/s. Thus, the impact of inertial forces, as observed in the numerical parametric study, is less likely to be observed in contaminant hydrology than gravity effects, and should be non-negligible for specific active mechanical remediation techniques or pipe rupture event in highly permeable porous media.

9. Conclusion

We studied experimentally the impact of gravitational and inertial forces on the injection of a model DNAPL (canola oil) into a wetting fluid (ethanol) in saturated highly permeable porous media. We conducted laboratory-scale injections in packing of glass beads of diameter 1 and 2 mm, with different injection flow rates and initial saturation (either fully saturated in ethanol or with an initial residual oil saturation). These experimental results, provided in the linked data repository, can be used as a simple benchmark for two-phase models.

Due to the high viscosity of the oil, the low interfacial tension, and the inlet condition, capillary effect can be considered as negligible and the displacement was mainly driven by viscous and gravity forces. Experiments showed (i) a gravity stabilized fluid front for each case, (ii) a strong impact of gravity forces which flattened the fluid front and laterally spread the injected oil, (iii) a small irreducible saturation in ethanol remaining in the oil zone (between 6% and 12%, depending on flow rates, and (iv) a sharp front displacement for each experiment.

This latter observation allowed us to use an arbitrary Lagrangian-Eulerian method, coupled with single-phase Darcy-Forchheimer equations, to reproduce the experiments and further investigate the impact of gravity and inertia forces on the flow process. We studied either an injection scenario similar to the experiments or a pumping scenario resembling experiments from Philippe et al. (2021). Based on the parametric studies, we found that the impact of gravity was most important from $0.1 \lesssim G_r$. This threshold value is low enough to be reached during most DNAPL flows encountered in contaminant hydrology. Gravity effects manifested themselves by flattening the fluid front, which is particularly visible in the injection scenario. Moreover, the observed behavior is consistent with the experiments, which further proves the interest in using dimensionless numbers obtained at Darcy-scale to study large-scale flow.

Macroscopic inertia effects (indicated with the Forchheimer number F_o) were non-negligible and increased faster from $F_o \approx 0.1$. These effects were mainly visible on the fluid front closer to the injection point, or further away from the pumping point, depending on the scenario, due to the increasing flow resistance from inertia. Such values are harder to reach in contaminant hydrology, but may occur for active mechanical remediation techniques in coarse sand, gravels, or other very coarse materials and involving low viscosity DNAPL (e.g. chlorinated solvents). More broadly, this work can be used to study the recovery of DNAPL as a pool in porous media (choice of DNAPL pumping rates or non-Newtonian liquid injection rates to recover DNAPL).

The impact of inertia forces was better highlighted using a different Initial Boundary Value Problem (IBVP) than for the impact of gravity. Whereas we tested different configurations (pumping, injection, constant inlet pressure, or constant inlet velocity), we have by no means exhausted all the possibilities. We have also only considered stable displacements in this study. Gravity or viscous instabilities are very common phenomena in the subsurface. For example, recent experiments by Philippe et al. (2020) have clearly shown that viscous fingering is important during DNAPL pumping with thermal enhancement. Consequently, further interesting and valuable work may consist of studying the impact of inertia and gravity on instabilities.

References

Abriola, L., Pinder, G.F., 1985. A multiphase approach to the modeling of porous media contaminated by organic compounds -1: Equation development. Water Resources Res 21, 11–18.

Ajo-Franklin, J., Geller, J., Harris, J., 2004. The dielectric properties of granular media saturated with dnapl/water mixtures. Geophysical Research Letters 31.

Anderson, W.G., et al., 1987. Wettability literature survey part 5: the effects of wettability on relative permeability. Journal of Petroleum Technology 39, 1–453.

Attou, A., Boyer, C., Ferschneider, G., 1999. Modelling of the hydrodynamics of the cocurrent gas–liquid trickle flow through a trickle-bed reactor. Chemical Engineering Science 54, 785–802.

Auriault, J., Sanchez-Palencia, E., 1986. Remarques sur la loi de darcy pour les écoulements biphasiques en milieu poreux. Journal of Theoretical and Applied Mechanics, Numéro Spécial , p141–156.

Avraam, D.G., Payatakes, A.C., 1999. Flow mechanisms, relative permeabilities, and coupling effects in steady-state two-phase flow through porous media. the case of strong wettability. Industrial & Engineering Chemistry Research 38, 778–786.

Bacri, J.C., Chaouche, M., Salin, D., 1990. Modèle simple de perméabilités relatives croisées. Comptes rendus de l'Académie des sciences. Série 2, Mécanique, Physique, Chimie, Sciences de l'univers, Sciences de la Terre 311, 591–597.

Barenblatt, G.I., Patzek, T.W., Silin, D.B., 2003. The mathematical model of nonequilibrium effects in water-oil displacement. SPE journal 8, 409–416.

Bear, J., Braester, C., Menier, P.C., 1987. Effective and relative permeabilities of anisotropie porous media. Transport in porous media 2, 301–316.

Birchak, J.R., Gardner, C.G., Hipp, J.E., Victor, J.M., 1974. High dielectric constant microwave probes for sensing soil moisture. Proceedings of the IEEE 62, 93–98.

Christie, M.A., Blunt, M., et al., 2001. Tenth spe comparative solution project: A comparison of upscaling techniques, in: SPE reservoir simulation symposium, Society of Petroleum Engineers.

Chuoke, R., Van Meurs, P., van der Poel, C., et al., 1959. The instability of slow, immiscible, viscous liquid-liquid displacements in permeable media. Transactions of the AIME 216, 188–194.

Clavier, R., Chikhi, N., Fichot, F., Quintard, M., 2017. Modeling of inertial multi-phase flows through high permeability porous media: Friction closure laws. International Journal of Multiphase Flow 91, 243–261.

Colombano, S., Davarzani, H., van Hullebusch, E., Huguenot, D., Guyonnet, D., Deparis, J., Ignatiadis, I., 2020. Thermal and chemical enhanced recovery of heavy chlorinated organic compounds in saturated porous media: 1d cell drainage-imbibition experiments. Science of The Total Environment 706, 135758.

Colombano, S., Davarzani, H., van Hullebusch, E., Huguenot, D., Guyonnet, D., Deparis, J., Ignatiadis, I., 2021a. Permittivity and electrical resistivity measurements and estimations during the recovery of dnapl in saturated porous media: 2d tank experiments. Journal of Applied Geophysics 191, 104359.

Colombano, S., Davarzani, H., van Hullebusch, E., Huguenot, D., Guyonnet, D., Deparis, J., Lion, F., Ignatiadis, I., 2021b. Comparison of thermal and chemical enhanced recovery of dnapl in saturated porous media: 2d tank pumping experiments and two-phase flow modelling. Science of The Total Environment 760, 143958.

Cueto-Felgueroso, L., Juanes, R., 2009. A phase field model of unsaturated flow. Water Resources Research 45, W10409.

Danis, M., Quintard, M., 1984. Modélisation d'un écoulement diphasique dans une succession de pores. Revue de l'Institut français du pétrole 39, 37–46.

Davit, Y., Quintard, M., 2019. One-phase and two-phase flow in highly permeable porous media. Heat Transfer Engineering 40, 391–409.

De Santos, J., Melli, T.R., Scriven, L., 1991. Mechanics of gas-liquid flow in packed-bed contactors. Annual review of fluid mechanics 23, 233–260.

DiCarlo, D.A., 2013. Stability of gravity-driven multiphase flow in porous media: 40 years of advancements. Water Resources Research 49, 4531–4544.

Dullien, F.A.L., Dong, M., 1996. Experimental determination of the flow transport coefficients in the coupled equations of two-phase flow in porous media. Transport in Porous Media 25, 97–120.

D'Aniello, A., Hartog, N., Sweijen, T., Pianese, D., 2018. Infiltration and distribution of elemental mercury dnapl in water-saturated porous media: experimental and numerical investigation. Water, Air, & Soil Pollution 229, 1–17.

Engelmann, C., Lari, K.S., Schmidt, L., Werth, C.J., Walther, M., 2021. Towards predicting dnapl source zone formation to improve plume assessment: Using robust laboratory and numerical experiments to evaluate the relevance of retention curve characteristics. Journal of Hazardous Materials 407, 124741.

Ergun, S., 1952. Fluid flow through packed columns. Chem. Eng. Prog. 48, 89–94.

Fetter, C.W., Boving, T.B., Kreamer, D.K., 1999. Contaminant hydrogeology. volume 500. Prentice hall Upper Saddle River, NJ.

Firdaouss, M., Guermond, J.L., Le Quéré, P., 1997. Nonlinear corrections to darcy's law at low reynolds numbers. Journal of Fluid Mechanics 343, 331–350.

Flemisch, B., Darcis, M., Erbertseder, K., Faigle, B., Lauser, A., Mosthaf, K., Müthing, S., Nuske, P., Tatomir, A., Wolff, M., et al., 2011. Dumux: Dune for multi-{phase, component, scale, physics,…} flow and transport in porous media. Advances in Water Resources 34, 1102–1112.

Forchheimer, P., 1901. Wasserbewegung durch Boden. Z. Ver. Deutsch. Ing. 45, 1782–1788.

Fourar, M., Lenormand, R., Larachi, F., 2001. Extending the f-function concept to two-phase flow in trickle beds. Chemical Engineering Science 56, 5987–5994.

Freeze, R.A., Cherry, J.A., 1979. Groundwater. Technical Report.

Ghane, E., Fausey, N.R., Brown, L.C., 2014. Non-darcy flow of water through woodchip media. Journal of Hydrology 519, 3400–3409.

Glass, R., Nicholl, M., 1996. Physics of gravity fingering of immiscible fluids within porous media: An overview of current understanding and selected complicating factors. Geoderma 70, 133–164.

Hassanizadeh, S.M., Gray, W.G., 1987. High velocity flow in porous media. Transport in porous media 2, 521–531.

Hassanizadeh, S.M., Gray, W.G., 1993. Thermodynamic basis of capillary pressure in porous media. Water resources research 29, 3389–3405.

Helmig, R., et al., 1997. Multiphase flow and transport processes in the subsurface: a contribution to the modeling of hydrosystems. Springer-Verlag.

Hill, R.J., Koch, D.L., Ladd, A.J., 2001. Moderate-reynolds-number flows in ordered and random arrays of spheres. Journal of Fluid Mechanics 448, 243.

Horgue, P., Soulaine, C., Franc, J., Guibert, R., Debenest, G., 2015. An open-source toolbox for multiphase flow in porous media. Computer Physics Communications 187, 217–226.

Hu, H.H., Patankar, N.A., Zhu, M., 2001. Direct numerical simulations of fluid–solid systems using the arbitrary lagrangian–eulerian technique. Journal of Computational Physics 169, 427–462.

Hu, K., Theofanous, T., 1991. On the measurement and mechanism of dryout in volumetrically heated coarse particle beds. International journal of multiphase flow 17, 519–532.

Ji, S.H., Lee, H.B., Yeo, I.W., Lee, K.K., 2008. Effect of nonlinear flow on dnapl migration in a rough-walled fracture. Water resources research 44.

Kalaydjian, F.M., et al., 1992. Dynamic capillary pressure curve for water/oil displacement in porous media: Theory vs. experiment, in: SPE Annual Technical Conference and Exhibition, Society of Petroleum Engineers.

Käser, D., Hunkeler, D., 2016. Contribution of alluvial groundwater to the outflow of mountainous catchments. Water Resources Research 52, 680–697.

Lake, L.W., 1989. Enhanced oil recovery .

Lasseux, D., Abbasian Arani, A.A., Ahmadi, A., 2011. On the stationary macroscopic inertial effects for one phase flow in ordered and disordered porous media. Physics of fluids 23, 073103.

Lasseux, D., Ahmadi, A., Arani, A.A.A., 2008. Two-phase inertial flow in homogeneous porous media: A theoretical derivation of a macroscopic model. Transport in porous media 75, 371–400.

Lasseux, D., Quintard, M., Whitaker, S., 1996. Determination of permeability tensors for two-phase flow in homogeneous porous media: theory. Transport in Porous Media 24, 107–137.

Lenormand, R., Touboul, E., Zarcone, C., 1988. Numerical models and experiments on immiscible displacements in porous media. Journal of fluid mechanics 189, 165–187.

Li, H., Pan, C., Miller, C.T., 2005. Pore-scale investigation of viscous coupling effects for two-phase flow in porous media. Physical Review E 72, 026705.

Lipinski, R.J., 1982. Model for boiling and dryout in particle beds. Technical Report. Sandia National Labs.

Ma, H., Ruth, D., 1993. The microscopic analysis of high forchheimer number flow in porous media. Transport in Porous Media 13, 139–160.

MacDonald, A., Maurice, L., Dobbs, M., Reeves, H., Auton, C., 2012. Relating in situ hydraulic conductivity, particle size and relative density of superficial deposits in a heterogeneous catchment. Journal of Hydrology 434, 130–141.

Macini, P., Mesini, E., Viola, R., 2011. Laboratory measurements of non-darcy flow coefficients in natural and artificial unconsolidated porous media. Journal of Petroleum Science and Engineering 77, 365–374.

Marle, C., et al., 1967. Ecoulements monophasiques en milieu poreux. Rev. Inst. Français du Pétrole 22, 1471–1509.

Marle, C.M., 1982. On macroscopic equations governing multiphase flow with diffusion and chemical reactions in porous media. International Journal of Engineering Science 20, 643 – 662.

Mei, C., Auriault, J.L., 1991. The effect of weak inertia on flow through a porous medium. Journal of Fluid Mechanics 222, 647–663.

Muskat, M., 1938. The flow of homogeneous fluids through porous media. Soil Science 46, 169.

Nofal, S., Travi, Y., Cognard-Plancq, A.L., Marc, V., 2019. Impact of infiltrating irrigation and surface water on a mediterranean alluvial aquifer in france using stable isotopes and hydrochemistry, in the context of urbanization and climate change. Hydrogeology Journal 27, 2211–2229.

Nsir, K., Schäfer, G., di Chiara Roupert, R., Razakarisoa, O., Toussaint, R., 2012. Laboratory experiments on dnapl gravity fingering in water-saturated porous media. International journal of multiphase flow 40, 83–92.

Odeh, A., 1959. Effect of viscosity ratio on relative permeability (includes associated paper 1496-g). Transactions of the AIME 216, 346–353.

Omirbekov, S., 2020. Polluted soil remediation using surfactant foam injection: experiments and upscaling. Ph.D. thesis. HESAM Université.

Or, D., 2008. Scaling of capillary, gravity and viscous forces affecting flow morphology in unsaturated porous media. Advances in water resources 31, 1129–1136.

Parlange, J.Y., Hill, D., 1976. Theoretical analysis of wetting front instability in soils. Soil Science 122, 236–239.

Pasquier, S., Quintard, M., Davit, Y., 2017. Modeling two-phase flow of immiscible fluids in porous media: Buckley-leverett theory with explicit coupling terms. Physical Review Fluids 2, 104101.

Philippe, N., Davarzani, H., Colombano, S., Dierick, M., Klein, P.Y., Marcoux, M., 2020. Experimental study of the temperature effect on two-phase flow properties in highly permeable porous media: Application to the remediation of dense non-aqueous phase liquids (dnapls) in polluted soil. Advances in Water Resources 146, 103783.

Philippe, N., Davarzani, H., Colombano, S., Dierick, M., Klein, P.Y., Marcoux, M., 2021. Experimental study of thermally enhanced recovery of high-viscosity dnapl in saturated porous media under non-isothermal conditions. Journal of Contaminant Hydrology , 103861.

Quintard, M., Whitaker, S., 1988. Two-phase flow in heterogeneous porous media: The method of large-scale averaging. Transport in porous media 3, 357–413.

Ramakrishnan, T.S., Goode, P.A., 2015. Measurement of off-diagonal transport coefficients in two-phase flow in porous media. Journal of colloid and interface science 449, 392–398.

Rao, R.K., Arnold, L.K., 1956. Alcoholic extraction of vegetable oils. iii. solubilities of babassu, coconut, olive, palm, rapeseed, and sunflower seed oils in aqueous ethanol. Journal of the american oil chemists society 33, 389–391.

Rothman, D.H., 1990. Macroscopic laws for immiscible two-phase flow in porous media: Results from numerical experiments. Journal of Geophysical Research 95, 8663.

Ruth, D., Ma, H., 1992. On the derivation of the forchheimer equation by means of the averaging theorem. Transport in Porous Media 7, 255–264.

Saffman, P.G., Taylor, G.I., 1958. The penetration of a fluid into a porous medium or hele-shaw cell containing a more viscous liquid. Proceedings of the Royal Society of London. Series A. Mathematical and Physical Sciences 245, 312–329.

de Santos, J.M., Melli, T.R., Scriven, L.E., 1991. Mechanics of gas-liquid flow in packed-bed contactors. Annual Review of Fluid Mechanics 23, 233–260.

Schneider, C.A., Rasband, W.S., Eliceiri, K.W., 2012. Nih image to imagej: 25 years of image analysis. Nature methods 9, 671–675.

Schulenberg, T., Müller, U., 1987. An improved model for two-phase flow through beds of coarse particles. International journal of multiphase flow 13, 87–97.

Schwartz, L., 1961. Méthodes mathématiques pour les sciences physiques .

Schwille, F., Pankow, J.F., 1988. Dense chlorinated solvents in porous and fractured media-model experiments .

Shams, M., Raeini, A.Q., Blunt, M.J., Bijeljic, B., 2018. A study to investigate viscous coupling effects on the hydraulic conductance of fluid layers in two-phase flow at the pore level. Journal of colloid and interface science 522, 299–310.

Sleep, B.E., Ma, Y., 1997. Thermal variation of organic fluid properties and impact on thermal remediation feasibility. Soil and Sediment Contamination 6, 281–306.

Theel, M., Huggenberger, P., Zosseder, K., 2020. Assessment of the heterogeneity of hydraulic properties in gravelly outwash plains: a regionally scaled sedimentological analysis in the munich gravel plain, germany. Hydrogeology Journal 28, 2657–2674.

Tung, V., Dhir, V., 1988. A hydrodynamic model for two-phase flow through porous media. International journal of multiphase flow 14, 47–65.

Van Genuchten, M.T., 1980. A closed-form equation for predicting the hydraulic conductivity of unsaturated soils. Soil science society of America journal 44, 892–898.

Vaudan, J., Parriaux, A., Tacher, L., Della Valle, G., 2005. Spécificités hydrogéologiques des hautes vallées alpines: Exemple de la haute-sarine (suisse). Eclogae Geologicae Helvetiae 98, 371–383.

Whitaker, S., 1986. Flow in porous media II: The governing equations for immiscible, two-phase flow. Transport in porous media 1, 105–125.

Whitaker, S., 1996. The forchheimer equation: a theoretical development. Transport in Porous media 25, 27–61.

Wilking, B.T., Rodriguez, D.R., Illangasekare, T.H., 2013. Experimental study of the effects of dnapl distribution on mass rebound. Groundwater 51, 229–236.

Wodie, J.C., Levy, T., 1991. Correction non linéaire de la loi de darcy. Comptes rendus de l'Académie des sciences. Série 2, Mécanique, Physique, Chimie, Sciences de l'univers, Sciences de la Terre 312, 157–161.

Yiotis, A.G., Psihogios, J., Kainourgiakis, M.E., Papaioannou, A., Stubos, A.K., 2007. A lattice boltzmann study of viscous coupling effects in immiscible two-phase flow in porous media. Colloids and Surfaces A: Physicochemical and Engineering Aspects 300, 35–49.

Yoon, H., Oostrom, M., Wietsma, T.W., Werth, C.J., Valocchi, A.J., 2009. Numerical and experimental investigation of dnapl removal mechanisms in a layered porous medium by means of soil vapor extraction. Journal of contaminant hydrology 109, 1–13.

Zarcone, C., Lenormand, R., 1994. Détermination expérimentale du couplage visqueux dans les écoulements diphasiques en milieu poreux. Comptes rendus de l'Académie des sciences. Série II, Mécanique, physique, chimie, astronomie 318, 1429–1435.

Zeng, Z., Grigg, R., 2006. A criterion for non-darcy flow in porous media. Transport in porous media 63, 57–69.

Zheng, F., Gao, Y., Sun, Y., Shi, X., Xu, H., Wu, J., 2015. Influence of flow velocity and spatial heterogeneity on dnapl migration in porous media:

insights from laboratory experiments and numerical modelling. Hydrogeology Journal 23, 1703–1718.

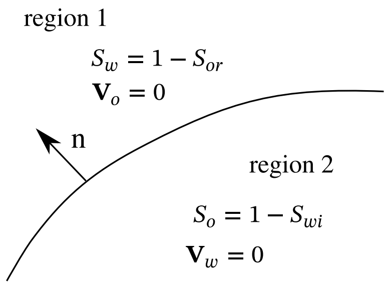

Figure A.19: Macroscopic front between the two fluids. Unit normal vector to the interface $\mathbf{n}$ is oriented from fluid o toward fluid w.

Appendix A. ALE boundary condition at the fluid front

We write Darcy equations for each phase, distributed as in Fig. A.19, as a departure to derive the boundary condition at the fluid front for the ALE model.

In region 1:

$$0 = \frac{\partial \phi S_w \rho_w}{\partial t} + \nabla \cdot \rho_w \mathbf{V}_w, \tag{A.1a}$$

$$\mathbf{V}_w = -\frac{\mathbf{K}_w}{\mu_w} \cdot \left(\nabla P_w - \rho_w \mathbf{g}\right). \tag{A.1b}$$

In region 2:

$$0 = \frac{\partial \phi (1 - S_w) \rho_o}{\partial t} + \nabla \cdot \rho_o \mathbf{V}_o, \tag{A.2a}$$

$$\mathbf{V}_o = -\frac{\mathbf{K}_o}{\mu_o} \cdot \left(\nabla P_o - \rho_o \mathbf{g}\right). \tag{A.2b}$$

The next step is to write a unique macroscopic momentum balance equation, written in sense of distributions (Schwartz, 1961), as

$$\mathbf{V}_\alpha = -\frac{\mathbf{K}_\alpha}{\mu_\alpha} \cdot \left(\{\nabla P_\alpha\} + [P] - \rho_\alpha \mathbf{g}\right), \tag{A.3}$$

where α refers to region 1 and 2, and $\{\nabla f\}$ indicates the gradient of function f in the sense of functions (usual gradient) and $[\cdot]$ the jump across the discontinuity interface. Here, we have

$$[P] = P_w - P_o = 0. \tag{A.4}$$

We treat the mass balance equation for each fluid w and o independently.

For fluid w:

$$\left\{\frac{\partial}{\partial t}\left(\phi S_{w\alpha}\rho_w\right)\right\} + \{\nabla \cdot (\rho_w \mathbf{V}_{w\alpha})\} = 0. \tag{A.5}$$

For fluid o:

$$\left\{\frac{\partial}{\partial t}\left(\phi(1 - S_{w\alpha})\rho_o\right)\right\} + \{\nabla \cdot (\rho_o \mathbf{V}_{o\alpha})\} = 0. \tag{A.6}$$

The associated jump discontinuity reads

$$-\phi\left[S_{w\alpha}\rho_\alpha\right]\mathbf{n}\cdot\mathbf{w} + \left[\rho_w \mathbf{V}_{w\alpha}\right]\cdot\mathbf{n} = 0, \tag{A.7}$$

for fluid w, and

$$-\phi\left[(1 - S_{w\alpha})\rho_o\right]\mathbf{n}\cdot\mathbf{w} + \left[\rho_o \mathbf{V}_{o\alpha}\right]\cdot\mathbf{n} = 0, \tag{A.8}$$

for fluid o and where $\mathbf{w}$ is the front velocity. We use the time derivative of a function on a discontinuity interface, in the sense of distributions,

$$\frac{\partial f}{\partial t} = \left\{\frac{\partial f}{\partial t}\right\} - [f]\,\mathbf{w}\cdot\mathbf{n}. \tag{A.9}$$

Since $\mathbf{V}_{w2} = 0$, $\mathbf{V}_{o1} = 0$, $S_{w1} = 1 - S_{or}$ and $S_{o2} = 1 - S_{wi}$, we can write

$$\mathbf{V}_{w1}\cdot\mathbf{n} = \phi(1 - S_{wi} - S_{or})\mathbf{n}\cdot\mathbf{w}, \tag{A.10}$$

$$\mathbf{V}_{o2}\cdot\mathbf{n} = \phi(1 - S_{wi} - S_{or})\mathbf{n}\cdot\mathbf{w}, \tag{A.11}$$

As **w** is unique, continuity of the velocity should be ensured, and the front velocity is finally expressed as

$$\mathbf{w} \cdot \mathbf{n} = \frac{1}{\phi(1 - S_{wi} - S_{or})} \mathbf{V} \cdot \mathbf{n}. \tag{A.12}$$